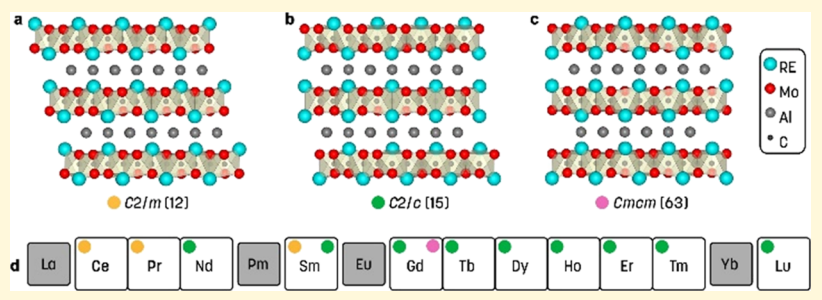


Atomically Layered and Ordered Rare-Earth i-MAX Phases: A New Class of Magnetic Quaternary Compounds

Quanzheng Tao,*,† Jun Lu,† Martin Dahlqvist,† Aurelija Mockute,†,‡ Stuart Calder,‡ Andrejs Petruhins,† Rahele Meshkian,† Oleg Rivin,*, Daniel Potashnikov, El'ad N. Caspi, Hagai Shaked, Andreas Hoser, Christine Opagiste, Rose-Marie Galera, Ruslan Salikhov, Ulf Wiedwald, Clemens Ritter, Andrew R. Wildes, Börje Johansson, Lars Hultman,† Michael Farle, Michel W. Barsoum, †, ♦ and Johanna Rosen*, †

Supporting Information



ABSTRACT: In 2017, we discovered quaternary i-MAX phases—atomically layered solids, where M is an early transition metal, A is an A group element, and X is C—with a $(M_{2/3}^1 M_{1/3}^2)_2 AC$ chemistry, where the M^1 and M^2 atoms are in-plane ordered. Herein, we report the discovery of a class of magnetic i-MAX phases in which bilayers of a quasi-2D magnetic frustrated triangular lattice overlay a Mo honeycomb arrangement and an Al Kagomé lattice. The chemistry of this family is (Mo_{2/3}RE_{1/3})₂AlC, and the rare-earth, RE, elements are Ce, Pr, Nd, Sm, Gd, Tb, Dy, Ho, Er, Tm, and Lu. The magnetic properties were characterized and found to display a plethora of ground states, resulting from an interplay of competing magnetic interactions in the presence of magnetocrystalline anisotropy.

Rare earth (RE)-containing solids exhibit a variety of magnetic and electronic ground states through hybridization between their 4f and conduction electrons. 1-3 Heavy fermion compounds, mostly based on Ce and Yb, are prototype systems for the study of quantum critical⁴ and collective quantum states.⁵ Other degrees of freedom, like orbital and valence, yield a variety of states of matter.^{6,7} For

example, Sm exhibits valence instabilities that play a significant role in the exotic, strongly correlated, behavior in Sm compounds such as SmOs₄Sb₁₂⁸ and SmB₆.

Received: December 23, 2018 Revised: March 5, 2019 Published: March 6, 2019



[†]Thin Film Physics Division, Department of Physics, Chemistry, and Biology (IFM), Linköping University, SE-581 83 Linköping, Sweden

^{*}Neutron Scattering Division, Oak Ridge National Laboratory, Oak Ridge, Tennessee 37831, United States

[§]Physics Department, Nuclear Research Centre - Negev, P.O. Box 9001, Beer Sheva 84190, Israel

Helmholtz-Zentrum Berlin fur Materialien und Energie, Berlin 14109, Germany

¹Faculty of Physics, Technion - Israeli Institute of Technology, Haifa 32000, Israel

[&]quot;Israel Atomic Energy Commission, P.O. Box 7061, Tel Aviv 61070, Israel

^VPhysics Department, Ben-Gurion University of the Negev, P.O. Box 653, Beer Sheva 84105, Israel

OInstitut Neel, CNRS, Univ. Grenoble Alpes, Grenoble INP, FR-38000 Grenoble, France

Faculty of Physics and Center for Nanointegration (CENIDE), University of Duisburg-Essen, 47057 Duisburg, Germany

Institut Laue-Langevin, BP 156, 38042 Grenoble Cedex 9, France

[&]amp;Department of Physics and Astronomy, Uppsala University, Box 516, SE-751 20 Uppsala, Sweden

Physics Department, Humboldt University, Zum Grossen Windkanal 6, D-12489 Berlin, Germany

Department of Materials Science and Engineering, Drexel University, Philadelphia, Pennsylvania 19104, United States

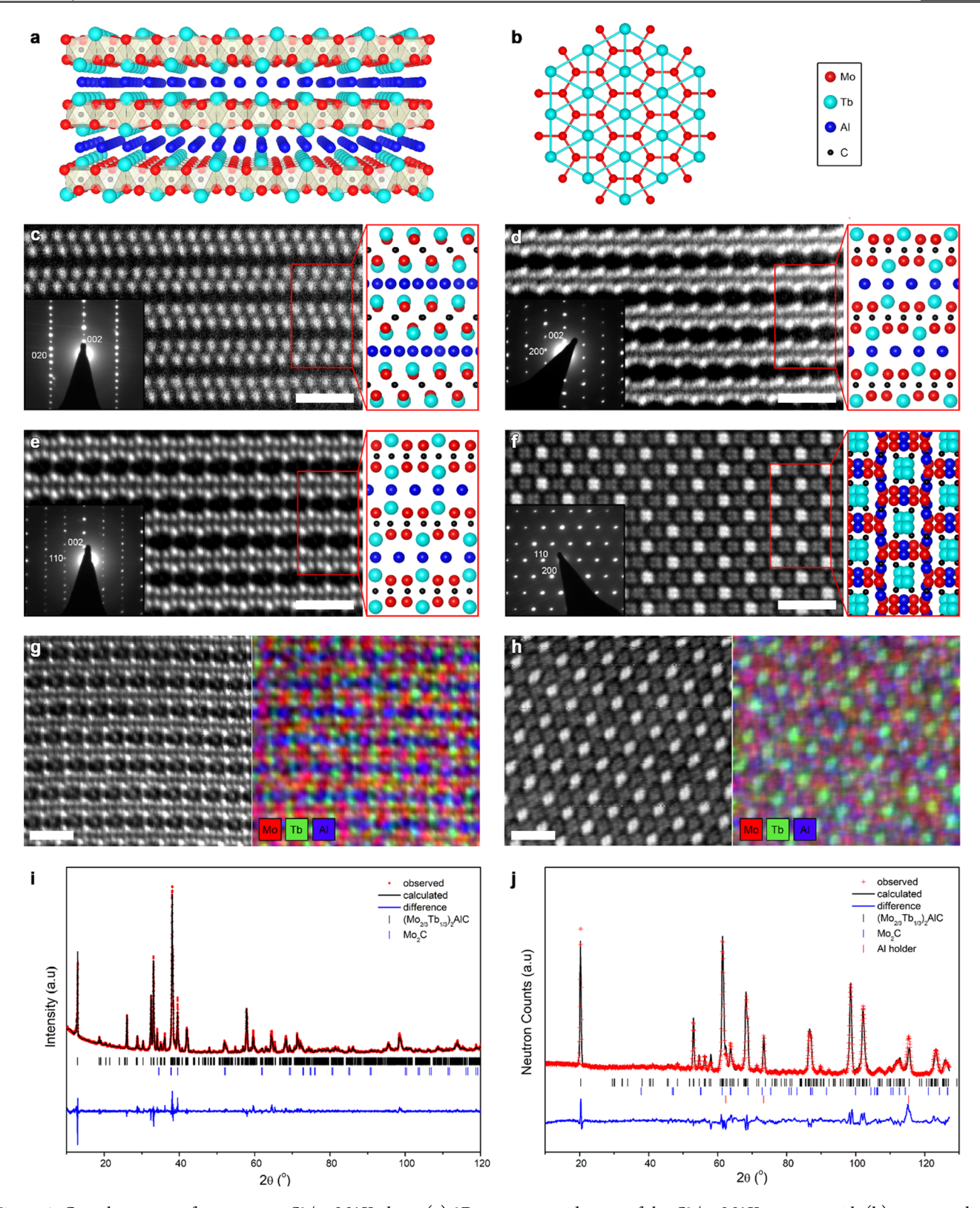


Figure 1. Crystal structure of space group C2/c *i*-MAX phase. (a) 3D perspective side view of the C2/c *i*-MAX structure with (b) corresponding top view of building block, $(Mo_{2/3}RE_{1/3})_2C$ layer. STEM images of $(Mo_{2/3}Tb_{1/3})_2AlC$ along (c) [100], (d) [010], (e) [110], and (f) [001] zone axes, with corresponding SAED. Schematics to the right of each panel represent the corresponding atomic arrangements assuming the structure is the space group C2/c (15). Atomic resolution EDX mapping of $(Mo_{2/3}Tb_{1/3})_2AlC$ along (g) [110] and (h) [100] zone axes. (i) Rietveld refinement of XRD pattern of $(Mo_{2/3}Tb_{1/3})_2AlC$ at room temperature. (j) Rietveld refinement of NPD pattern of $(Mo_{2/3}Tb_{1/3})_2AlC$ at 100 K. Scale bar (c-h), 1 nm.

While the collective magnetic response of RE ions is also influenced by the crystal structure and chemical environment,

we propose to probe for such effects in the $M_{n+1}AX_n$ phases, where M is an early transition metal (that as shown here can be

partially substituted with a RE), A is an A group element (mostly 13 and 14), and X is C and/or N. These so-called MAX phases are a class of atomically laminar materials. Most common examples are carbides and nitrides, ¹⁰ combining the characteristics of metals and ceramics. ¹¹ The rich chemistry of these materials renders them promising for applications ranging from structural materials at extreme conditions, ¹² ohmic contact materials for semiconductors, ¹³ and as precursors for their 2D counterparts, that is, MXenes. ^{14,15}

Recently, we discovered quaternary $(M^1_{2/3}, M^2_{1/3})_2AC$ phases that we coined *i*-MAX because the M elements are in-plane ordered. The M^1 atoms sit on a honeycomb lattice, and the M^2 atoms sit on a triangular lattice. The A layers form Kagomé-like patterns. This discovery has greatly expanded the number of M elements and their combinations that can be incorporated in the MAX phases. Examples include $(Mo_{2/3}Sc_{1/3})_2AlC$, $(Mo_{2/3}Y_{1/3})_2AlC$, $(V_{2/3}Zr_{1/3})_2AlC$, 16,17 and $(W_{2/3}Sc_{1/3})_2AlC$. Furthermore, selective etching of these phases allows for atomic scale engineering of ordered vacancies in the 2D nanosheet. 16,18

Herein, we report the synthesis of 11 new i-MAX phases with the general formula $(M_{2/3}^1, M_{1/3}^2)_2$ AlC, where M^1 is Mo and M² is a RE element, namely, Ce, Pr, Nd, Sm, Gd, Tb, Dy, Ho, Er, Tm, and Lu. In all cases, the resulting structure is layered with chain-like arrangement of the RE element (Figure 1a). When the metal layers are imaged from the top, it is clear that the RE atoms (depicted in cyan in Figure 1b) form a 2D triangular lattice. The here demonstrated frustrated quasi-2D sheets of RE elements are expected to lead to complex magnetic properties via intra- and interplane exchanges caused by the well-known Ruderman-Kittel-Kasuya-Yosida indirect coupling mechanism of localized inner 4f-shell electron spins through the conduction electrons. As shown here, the interplay of competing magnetic interactions in the presence of magnetocrystalline anisotropy gives rise to different magnetic properties. The purpose of this work is to describe the synthesis and structural and magnetic characteristics of these new i-MAX phases.

■ MATERIALS AND METHODS

Material Synthesis. Polycrystalline $(Mo_{2/3}RE_{1/3})_2AlC$ samples were synthesized by pressureless sintering the following elemental powders: graphite (99.999%), Mo (99.99%) from Sigma-Aldrich, Al (99.8%) from Alfa Aesar, and RE (99.9%) from Stanford Advanced Materials. Stoichiometric amounts of the elemental powders were manually mixed in an agate mortar and placed in an alumina crucible that was in turn inserted in an alumina tube furnace through which 5 sccm Ar was flowing. The furnace was then heated at 5 °C min⁻¹ up to 1500 °C and held at 1500 °C for 10 h, before furnace cooling to room temperature (RT). The loosely sintered powders were crushed into a fine powder that was directly used for further analysis.

Structural Characterization. X-ray diffraction (XRD) was carried out on a PANalytical X'Pert powder diffractometer with a Cu source ($\lambda_{K\alpha} \approx 1.54$ Å). Scanning transmission electron microscopy (STEM) combined with high angle annular dark field imaging (STEM-HAADF) and energy-dispersive X-ray spectroscopy (EDX) analysis with a Super-X EDX detector was performed in the double-corrected Linköping FEI Titan³ operated at 300 kV. Selected area electron diffraction (SAED) was performed on a FEI Tecnai T20 TEM operating at 200 kV.

Magnetization Measurements. The powders' magnetic properties were examined in magnetic fields up to ±9 T at variable temperatures using a vibrating sample magnetometer in a Quantum Design DynaCool Physical Property Measurement System (PPMS).

Heat Capacity Measurements. In the 2–100 K temperature range, the specific heat $(c_{\rm p})$ was measured using the relaxation method with a Quantum Design PPMS. The transition temperatures were deduced from inflection points of the anomalies. A tentative determination of the magnetic entropy $(S_{\rm M})$ from the experimental $c_{\rm p}$ was performed for RE = Tb. This was done to determine the degeneracy of the magnetic ground state. It is expected that the crystal electric field (CEF) interactions partly lift the 2J+1 degeneracy of the fundamental multiplet. Thus, it is necessary to properly subtract the phonon contribution from the total $c_{\rm p}$ in order to obtain the magnetic contribution $c_{\rm mag}$. For these compounds the phonon contribution were determined from $c_{\rm p}$ curves measured for the nonmagnetic (Mo_{2/3}Lu_{1/3})₂AlC. The $S_{\rm M}$ was obtained by integrating $c_{\rm mag}/T$ from 0 K to T. Since the lowest temperature reached in the present measurements was 2 K, it is likely that $S_{\rm M}$ is underestimated here.

Neutron Powder Diffraction. Neutron powder diffraction (NPD) measurements of (Mo_{2/3}Tb_{1/3})₂AlC were carried out using the HB-2A high-flux powder diffractometer at the High Flux Isotope Reactor at Oak Ridge National Laboratory (ORNL, USA). A 5 g powder sample was loaded in an Al cylindrical sample holder. Measurements were performed with a $\lambda = 2.41$ Å neutron wavelength produced by the (113) reflections from a vertical focusing Ge monochromator. $(Mo_{2/3}Tb_{1/3})_2AlC$ was measured at 1.5, 8, 15, 22, and 100 K. The data were collected using a ³He detector bank covering a 2θ range of $7-133^{\circ}$ in steps of 0.05° . The magnetic structures were determined using the following procedure: The additional peaks below the ordering temperature were fitted by a Gaussian function to find the peak position and corrected for zerooffset. The propagation vectors were searched using FullProf "ksearch". The symmetry analysis was performed by the FullProf "BasIreps". Finally, the spin configuration was determined by considering all possible magnetic models.

The high flux E6 neutron diffractometer, located at the Helmholtz-Zentrum Berlin (HZB, Germany), was used to obtain NPD profiles of $(\text{Mo}_{2/3}\text{Er}_{1/3})_2\text{AlC}$ at 298(2), 22(1), and 1.5(3) K. An incident beam $(\lambda \sim \! 2.4 \text{ Å})$ was obtained using a focusing pyrolytic graphite monochromator. A 4 g powder sample was loaded into a 6 mm diameter vanadium (V) cylindrical sample holder. Determination of the magnetic structure was carried out by using the SARAh package followed by a symmetry analysis with the BasIreps code. A systematic scan of the special propagation vectors in the Brillouin zone followed by a search along symmetry lines and planes combined with a Monte Carlo refinement of the magnetic structure was performed until a suitable propagation vector was found. Finally, the refinement was performed on the 1.5 K data by considering all possible magnetic models.

Theoretical Calculations. All calculations were performed within the framework of the density functional theory (DFT) as implemented in the Vienna ab initio simulation package 19-21 using the projector augmented wave method^{22,23} with spin-polarized generalized gradient approximation as parametrized by Perdew-Burke-Ernzerhof²⁴ for treating electron exchange and correlation effects. Wave functions were expanded in plane waves up to an energy cutoff of 400 eV, and the sampling of the Brillouin zones was carried out using the Monkhorst-Pack scheme.²⁵ We used two different treatments of the 4f electrons: (i) in core, or (ii) as part of the valence band, denoted 4f-core and 4f-band, respectively, henceforth. For the latter case, the degree of localization of the 4f electrons is important and needs to be considered. As a first approximation, we therefore used the rotationally invariant approach as proposed by Dudarev et al.²⁶ Note that within this formalism, the onsite Coulomb parameter U and the exchange parameter J are spherically averaged into a single effective interaction parameter $U_{\text{eff}} = U - J$, which does not depend on their individual values. Since the degree of localization for the 4f electrons is unknown, we chose to use different values of $U_{\rm eff}$ over the lanthanide series with a focus on $U_{\rm eff}$ = 3 or 7 eV. As a first approximation, we modeled the magnetism in $(Mo_{2/3}RE_{1/3})_2AIC$ within a collinear framework. The collinear magnetic spin configurations considered are visualized in Figure S4. The equilibrium structures are obtained by minimization of the total energy with

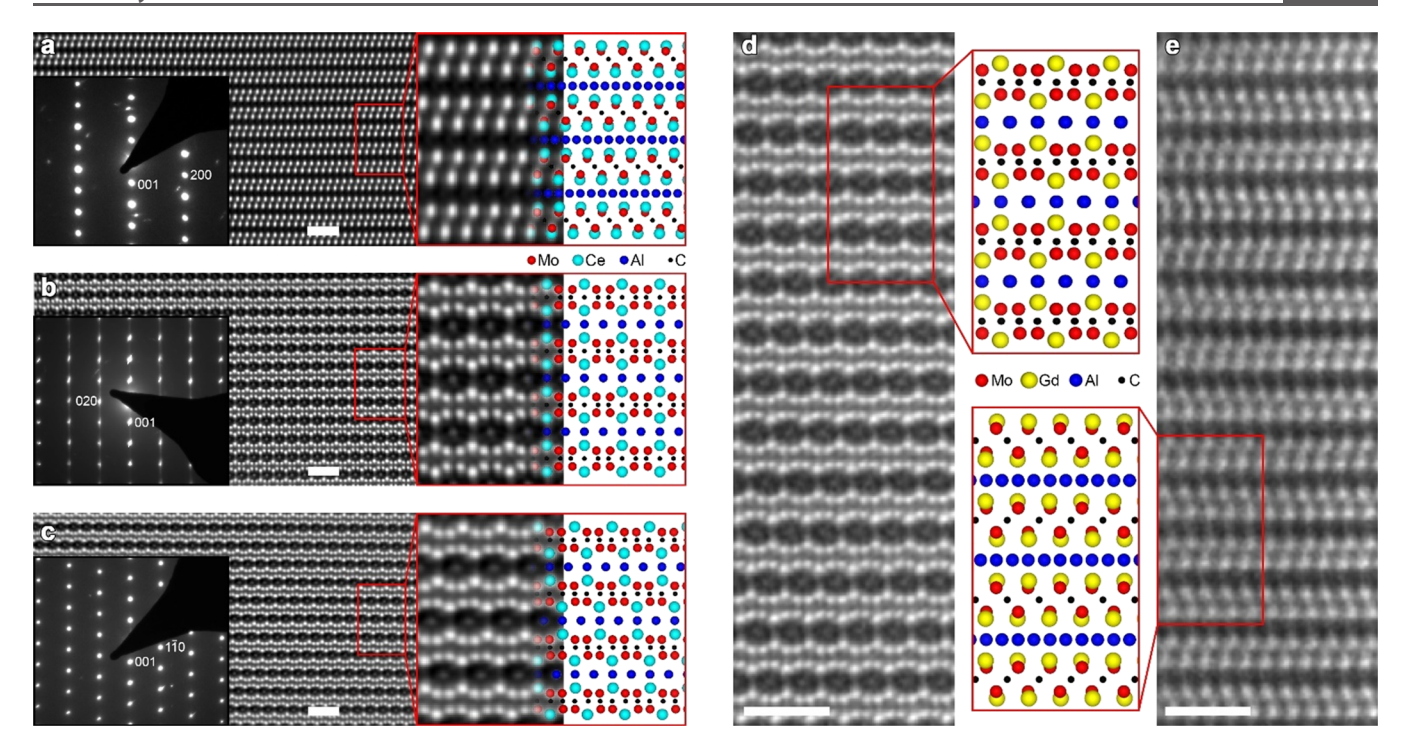


Figure 2. Crystal structure of the *i*-MAX phases. STEM images of $(Mo_{2/3}Ce_{1/3})_2AlC$ along (a) [010], (b) [100], and (c) [110] zone axes, with corresponding SAED. Schematics to the right of each panel represent the corresponding atomic arrangements assuming the structure is the space group C2/m (12). STEM images of $(Mo_{2/3}Gd_{1/3})_2AlC$ along (d) [110] and (e) [100] zone axes. Schematics to the right of each panel represent the corresponding atomic arrangements assuming the structure is the orthorhombic space group Cmcm (63). Scale bar, 1 nm.

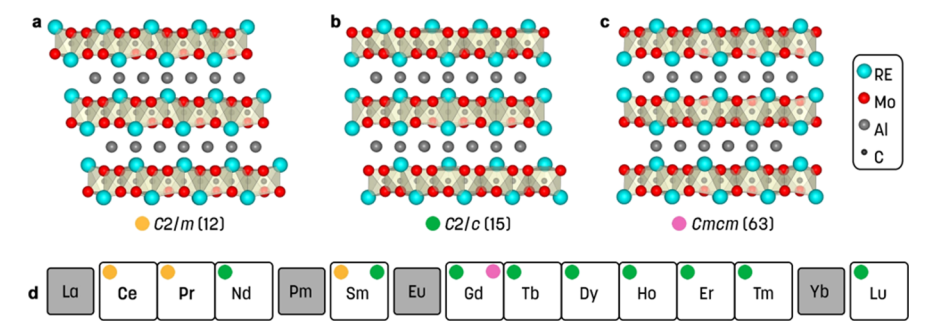


Figure 3. Summary of crystal structures of the *i*-MAX phases. Schematic of $(Mo_{2/3}RE_{1/3})_2AlC$ crystallized in (a) monoclinic C2/m, (b) monoclinic C2/c, and (c) orthorhombic Cmcm. (d) RE = Ce and Pr crystallize in C2/m, and RE = Nd, Tb, Dy, Ho, Er, Tm, and Lu crystallize in C2/c. Two polymorphs are found for RE = Sm and Gd.

respect to volume and with full relaxation of atomic positions and unit cell parameters until forces are converged below 10^{-3} eV Å⁻¹.

RESULTS

Crystal Structure and In-Plane Chemical Order. The synthesis of these phases is summarized in the Materials and Methods section. STEM and SAED were used for structural characterization and space group identification. XRD Rietveld refinements were used to determine the crystal structures and sample purity. Neutron powder diffraction (NPD) was used to correlate crystallographic and magnetic structures in selected compounds. Three polymorphs were identified with symmetries C2/c, C2/m, and Cmcm, represented by the Tb, Ce, and Gd i-MAX phases, respectively. Henceforth, for the sake of brevity, the various phases will simply be referred to by their RE element.

The Tb phase was the one with the highest sample purity and was chosen to depict the C2/c structure. Figure 1c-f shows STEM images of Tb along the [100], [010], [110], and

[001] zone axes, respectively. The Tb atoms appear brightest due to their large atomic number (Z contrast); Mo and Al are less bright; the lightest element, C, is not visible. The structure viewed along [100] looks identical to a traditional MAX phase viewed along [11-20]. In-plane Mo and Tb chemical orderings are evidenced by the [010] and [110] zone axes, with the Tb atoms extending from the M layers toward the Al layers, a general feature of most i-MAX phases. 16 Furthermore, the nonuniform Al atomic distribution (Figure 1g) originates from a Kagomé-like ordering in the Al layer. The SAED patterns (insets in Figure 1c-f) are consistent with monoclinic symmetry. The atomic arrangements, characteristic of monoclinic symmetry, determined by DFT, are shown as insets on the right of Figure 1c-f. The agreement between the STEM images and those predicted by DFT is excellent, confirming the chosen structure. The atomic arrangements of the Mo, Tb, and Al atoms are revealed in real space in the atomic resolved EDX mapping of these elements, shown on the right of Figure 1g,h. In the [110] map (Figure 1g), the

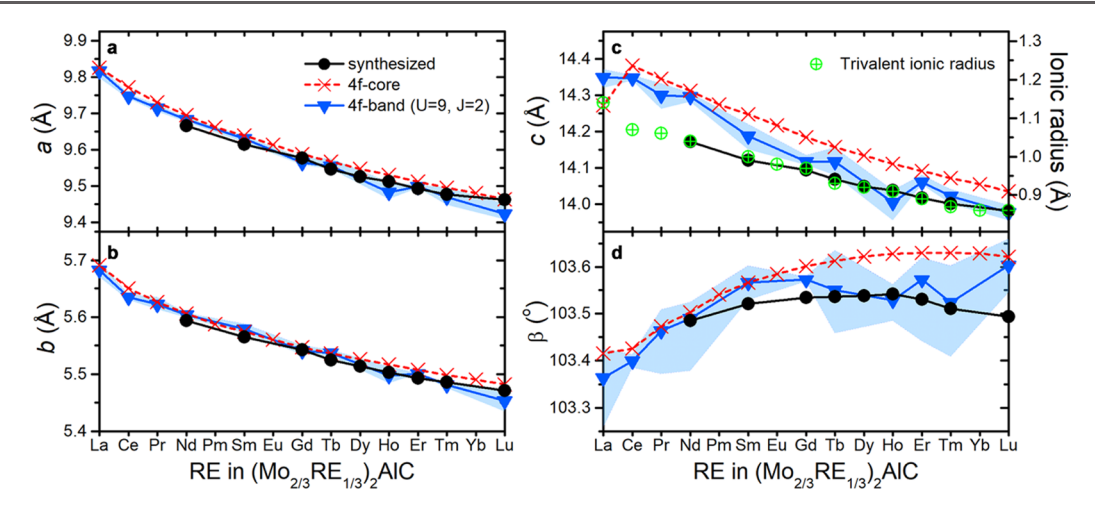


Figure 4. Structural parameters and magnetic properties. Measured (solid circles determined from XRD at RT) and calculated lattice parameters (red crosses and blue triangles) (a) a, (b) b, (c) c, and (d) angle β for $(Mo_{2/3}RE_{1/3})_2AIC$ crystallized in C2/c. Theoretical data are obtained by treating 4f electrons in the core (4f-core, red crosses) or as part of the valence band (4f-band, blue triangles). For the 4f-band we used U = 9 eV and U = 1 eV. Data points for the 4f-band are given as averaged value obtained for the lowest energy spin states, within 2 meV/atom, and corresponding min and max values are represented by the blue shaded area. The ionic radii of trivalent RE cations are included in panel (c) for comparison.

green dots represent individual Tb columns; in the [001] map (Figure 1f), they represent four Tb columns.

Rietveld refinement of the XRD pattern of the Tb phase (Figure 1i) confirmed the C2/c structure (see Table S1). The NPD pattern of the same phase at 100 K (Figure 1j) is also fully consistent with the XRD and STEM analyses and reveals full occupancy of the Mo and Tb sites with no intermixing. We thus conclude that the Tb atoms form a close to perfect triangular lattice.

The STEM images of the Ce phase (Figure 2a–c) are consistent with the C2/m symmetry. Similar to Tb, the Ce atoms appear brightest, with Ce extending from the M plane toward Al. Last, the STEM images of the Gd phase (Figure 2d,e) are consistent with the *Cmcm* symmetry and display the same characteristic features as its Tb and Ce counterparts. STEM images of the Pr-, Nd-, Sm-, Gd-, Dy-, Ho-, Er-, Tm-, and Lu-containing *i*-MAX phases are shown in Figure S1. The XRD results are shown in Figure S2, and the sample/structural information from refinement is listed in Tables S1 and S2 in Section S1.

Figure 3 summarizes our results: The Ce- and Pr-containing i-MAX phases crystallize in the C2/m structure; the Tb, Nd, Gd, Dy, Ho, Er, and Tm phases are C2/c. The Gd phase crystallizes in both Cmcm and C2/c. For the Sm phase, C2/m and C2/c structures coexist. Note that the C2/m structure is preferred for the lighter elements (to the left in Figure 3), while C2/c is preferred by the heavier ones (right).

Figure 4a–d compares the experimental (solid circles) and DFT predicted (crosses and triangles) lattice parameters (LPs) a, b, and c and the monoclinic angle β for the nine phases with the space group C2/c, showing that the LPs decrease with increasing 4f electrons. This behavior is in line with the lanthanide contraction. The monoclinic angle β is rather constant at ~103.5°.

As noted above, the DFT calculations were carried out with one of two assumptions. The first treats the 4f electrons as part of the core (red crosses in Figure 4a–d). The second treats the 4f electrons as a band (inverted blue triangles in Figure 4a–d). In both cases, the overall agreement between theory and experiment is good for the a and b LPs. Theory, however, overestimates the c LPs and angle β (Figure 4c,d). The absence

of data for Eu, Yb, and Pm reflects the fact that they were not realized experimentally.

The 4f-band model reproduces the LP trend well, with the largest relative difference for c (-0.1 to +0.9%) compared to the experimental values. As a first approximation, collinear spin configurations were assessed, and for a majority of the RE elements (Ce, Pr, Nd, Sm, Gd, Dy, Ho, Er, Tm), different spin states were accessible. For each spin state, the initially assigned spin configurations, shown in Figure S4, are degenerate in energies within 2 meV/atom. Calculated structural parameters are therefore presented in Figure 4a-d as average, maximum, and minimum values for the degenerate spin configurations corresponding to the spin state of lowest energy. The maxima and minima are represented by a blue band in Figure 4a-d. A closer examination of the calculated local magnetic moments of the RE elements, shown in Figure S5 for attained spin states from the 4f-band model, shows the largest moments for Gd (7 $\mu_{\rm B}$).

Magnetic Properties. The temperature (T) and magnetic field (H) dependencies of the magnetization (M) of the Ce, Pr, Nd, Sm, Gd, Tb, Dy, Ho, Er, and Tm phases were measured. Except for Sm and Tm, all compounds show long range magnetic order at temperatures ranging from 3.6 K for Er to 28 K for Tb (see Table 1). Figure S6 plots the inverse susceptibility $1/\chi$ (deduced from Arrott plots²⁹) or H/M versus T for the nine phases. In all cases but Sm, the transition to a magnetically ordered state follows a Curie–Weiss (C-W) law of the form

$$\chi = C/(T - \theta) \tag{1}$$

where C is the Curie constant and θ is the C–W temperature. From the slopes, the effective moment $\mu_{\rm eff}$ per RE atom is estimated (see Section S4). The parameters deduced from magnetometry are summarized in Table 1. The C–W temperatures vary, with the highest absolute values of about 20 K for Gd. The effective magnetic moments $\mu_{\rm eff}$ per RE atom rise from 3.6 $\mu_{\rm B}$ for Pr to 10.5 $\mu_{\rm B}$ for Dy and then decrease to $\mu_{\rm eff}$ = 7.32 $\mu_{\rm B}$ for Tm. For most phases, the Weiss temperatures are negative, reflecting antiferromagnetic interaction in these phases. Magnetization at 9 T shows similar trends for the effective moments. Generally, M is much reduced compared to

| Table 1. Parameters from Curie-Weiss | Fitting and |
|--------------------------------------|-------------|
| Magnetization Measurements | |

| RE | $T_{\rm N}$ or $T_{\rm C}$ (K) | $\Theta(K)$ | $\mu_{\mathrm{eff}}~(\mu_{\mathrm{B}})$ | $M_{ m 9T}~(\mu_{ m B})$ | $p (\mu_{\rm B})$ |
|----|--------------------------------|------------------|---|--------------------------|-------------------|
| Pr | 17.0 | 4.3 ^a | 3.58 ^a | 1.50 | 3.58 |
| Nd | 7.6 | -9.3 | 3.73 | 1.60 | 3.62 |
| Sm | | | | 0.03 | 0.85 |
| Gd | 26.0 | -20.3 | 8.34 | 2.14 | 7.94 |
| Tb | 20.1/28.0 | -12.1 | 9.70 | 3.40 | 9.72 |
| Dy | 13.3/16.0 | -1.0^{a} | 10.51 ^a | 6.74 | 10.63 |
| Ho | 7.8 | -4.5 | 10.28 | 5.60 | 10.60 |
| Er | 3.6 | 7.5 ^a | 9.24 ^a | 6.06 | 9.59 |
| Tm | | 6.2 ^a | 7.32 ^a | 4.30 | 7.57 |
| | | | | | |

"Values obtained from H/M versus T plots. Otherwise, they are obtained from $1/\chi$ versus T, in which χ is obtained from the Arrott plot. p (μ B) was calculated according to Hund's rule.

theoretical values. For some materials, like Tb and Er, the reduction is attributed to a CEF effect. For Tb, Dy, and Gd, the *M*'s do not reach saturation at 9 T. The *M* of Sm is extremely weak. The magnetic behaviors of possible impurities are summarized in Section S1 to exclude their potential contribution to the measured data.

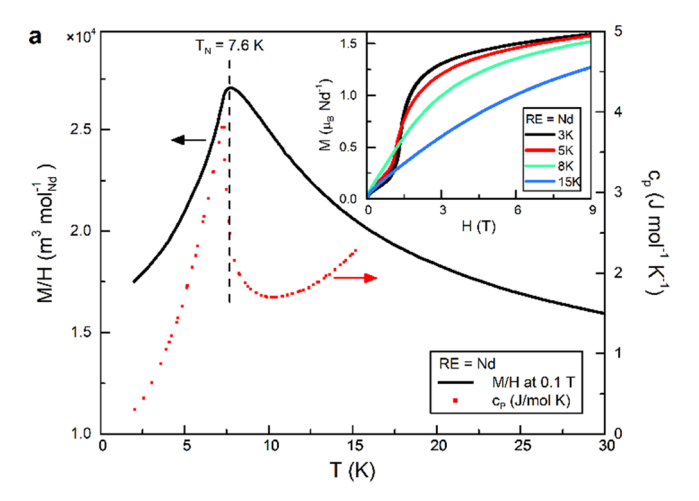
To exemplify the diversity and richness of the magnetic responses, four compounds, Nd, Gd, Tb, and Er, were selected for a more detailed magnetic analysis.

Each is presented separately in what follows.

 $(Mo_{2/3}Nd_{1/3})_2AIC$. In Figure 5a, the M/H versus T curve displays a distinct peak labeled $T_{\rm N}$ at 7.6 K, indicating a phase transition. Consistent with the magnetization data, a pronounced lambda anomaly in the heat capacity c_p is observed at ~ 8 K (right y-axis in Figure 5a). Plots of M(H)are shown in the inset of Figure 5a. While at higher temperature M shows Langevin-type paramagnetic behavior, there is a field-induced transition below T_N at around 1 T. The magnetization at 3 K reaches $\sim 1.6 \mu_B/Nd$ at 9 T, which is about half of the theoretical saturated moment (3.27 $\mu_{\rm B}$). The reduced moment is likely attributed to the CEF effect. 30 From the results shown in Figure S6b, the effective moment in the paramagnetic state is estimated to be $\mu_{\text{eff}} = 3.73(3) \mu_{\text{B}}$. This is close to the free ion value of Nd³⁺ (3.62 μ_B). The extrapolated negative temperature $\theta = -9.3$ K indicates AFM correlation between the Nd atoms.

 $(Mo_{2/3}Gd_{1/3})_2AlC$. The H/M curve measured under 0.1 T together with the inverse susceptibility $(1/\chi)$ deduced from Arrott plots is shown in Figure S6d. Both curves are consistent with the C–W law above 50 K; below they deviate upon cooling. The deviation may be attributed to short-range AFM correlations for T < 50 K. Note that Tb behaves similarly below 50 K (Figure S6e). This suggests that short-range AFM ordering is probably a general feature in the i-MAX series. Extracted information from the fitting gives a $\mu_{\rm eff}$ of 8.34 $\mu_{\rm B}/$ Gd, which is comparable to its free ion value of 7.94 $\mu_{\rm B}$. A negative C–W temperature θ of –20.3 K supports the AFM correlations in this phase. Magnetization increases almost linearly and shows no sign of saturation up to 9 T. Magnetization reaches 2.14 $\mu_{\rm B}/{\rm Gd}$ at 9 T.

The M/H versus T curve for Gd (left y-axis in Figure 5b) displays a small bump at $T_{\rm N}=26$ K, which neither shows a temperature hysteresis nor a split between zero field and field cooled curves. Moreover, the bump does not shift with increasing H; it just gets more pronounced (Figure S7a). To link the observed bump to changes in the electronic structure,



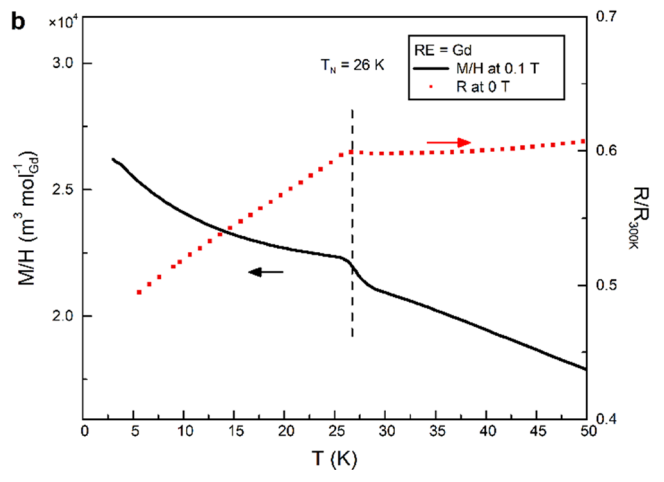


Figure 5. Magnetic properties. (a) Magnetization and specific heat c_p versus T for $(Mo_{2/3}Nd_{1/3})_2AlC$. (b) Magnetization and resistivity versus T for $(Mo_{2/3}Gd_{1/3})_2AlC$.

we measured the temperature dependence of the electrical resistance R. The results are shown in Figure S7b. From 300 to 50 K the response is metallic-like in that the resistance decreases linearly with decreasing temperatures. From 50 to 26 K, R (plotted on right y-axis in Figure 5b as a ratio to R at 300 K) levels off. Below 26 K, R decreases linearly again until 5 K. The sharp deflection on the R(T) curve at 26 K supports a distinct magnetic transition. The latter can also be seen from Arrott plots above and below $T_{\rm N}$. Above $T_{\rm N}$, the Arrott plots are linear (Figure S7c). Below $T_{\rm N}$ (Figure S7d), inflections can be seen at 15 and 20 K. Overall, we conclude that the Gd phase crosses a magnetic transition at a $T_{\rm N}$ of 26 K.

 $(Mo_{2/3}Tb_{1/3})_2AlC$. The functional dependence of M/H versus T curves on H is shown in Figure 6a (left y-axis). Below 1 T, a sharp AFM transition at 20 K denoted as $T_{\rm N1}$ is observed. The AFM ordering is also supported by M(H) curves that show field-induced transitions, marked with arrows, at 2 K (Figure 6c). Here another faint anomaly can be seen at 28 K henceforth referred to as $T_{\rm N2}$, marked with an arrow in Figure 6a. The temperature dependence of $c_{\rm p}$ (right y-axis in Figure 6a) clearly shows two lambda anomalies at $T_{\rm N1}$ and $T_{\rm N2}$ in zero field. Field dependent $c_{\rm p}$ measurements (Figure 6b) show that the anomaly at $T_{\rm N1}$ shifts toward lower T with increasing H, which disappears above 5 T. The anomaly at $T_{\rm N2}$ also shifts progressively to lower T; however, as opposed to $T_{\rm N1}$, $T_{\rm N2}$ is rather robust up to 9 T.

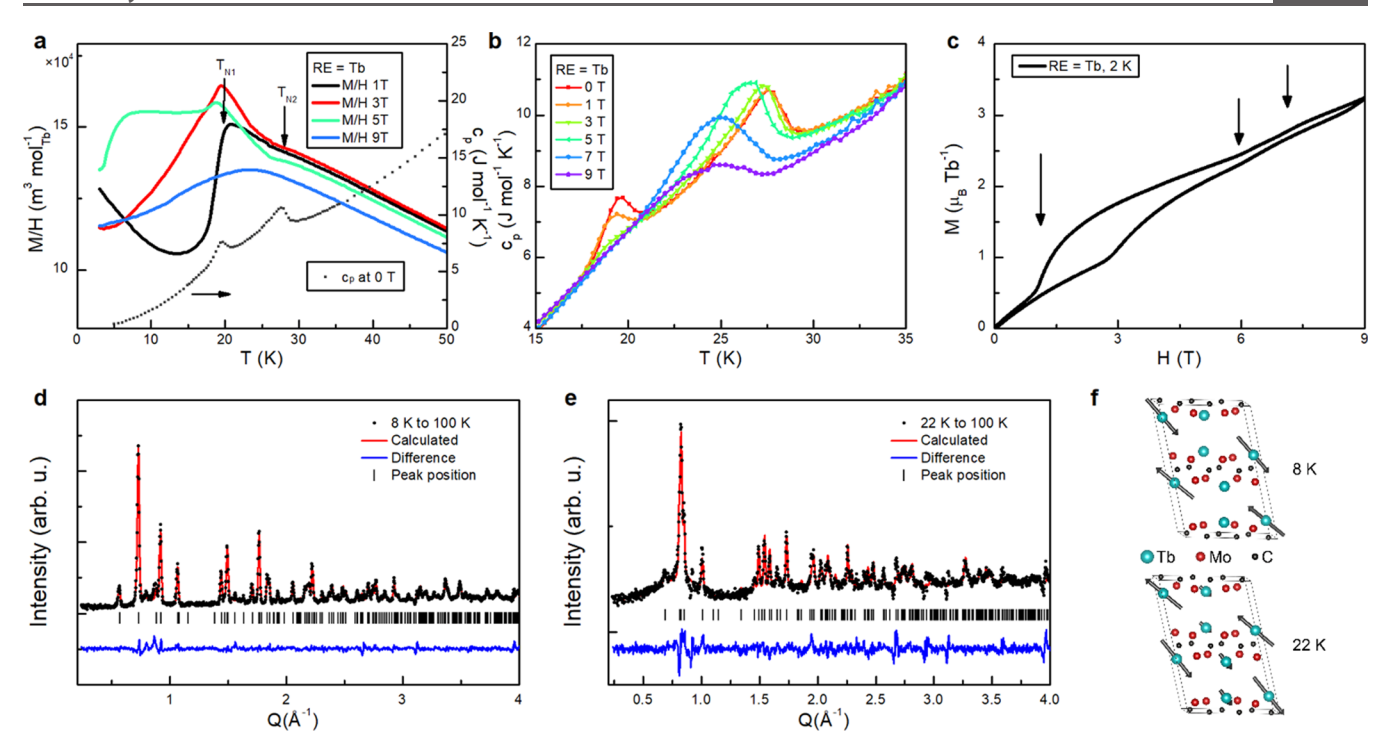


Figure 6. Magnetic properties of $(Mo_{2/3}Tb_{1/3})_2AlC$. (a) M/H versus T as a function of H and c_p versus T at 0 T. (b) c_p versus T as a function of H. (c) M versus H. Vertical arrows indicate field-induced transitions. (d) Magnetic scattering at 8 K obtained by subtracting the pattern at 100 K and its refinement. (e) Neutron magnetic scattering at 22 K obtained by subtracting the pattern at 100 K and its refinement. (f) Schematic of magnetic structures at 8 and 22 K. Al atoms are not shown for clarity.

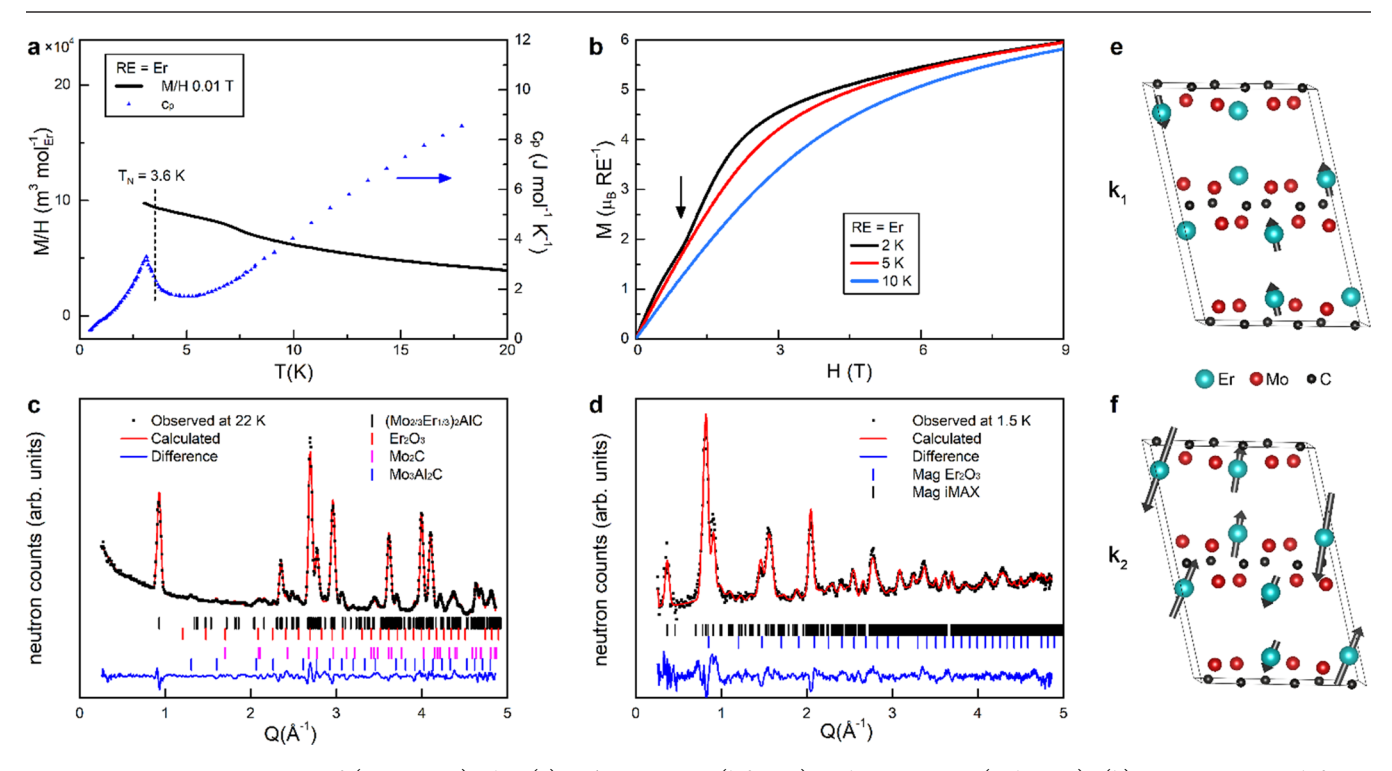


Figure 7. Magnetic properties of $(Mo_{2/3}Er_{1/3})_2AlC$. (a) M/H versus T (left axis) and c_p versus T (right axis). (b) M versus H at different temperatures. (c) NPD above T_N at 22 K. (d) Neutron magnetic scattering at 1.5 K. (e,f) Schematics of k_1 and k_2 magnetic structures.

To evaluate the CEF effect, we evaluated the magnetic entropy $S_{\rm M}$ by subtracting $c_{\rm p}$ of the nonmagnetic Lu compound from $c_{\rm p}$ of the Tb phase (see Figure S8a). The estimated $S_{\rm M}$ is shown in Figure S8b and reaches R ln 2 around 24 K, where R is the ideal gas constant. The Tb³⁺ ion is a non-Kramers ion,

and CEF interactions lift the degeneracy of the J=6 ground state multiplets into singlets. The value of $S_{\rm M}$ suggests that the first excited level is quite close to the ground state.

The M versus H curves for the Tb phase in the 2 to 50 K temperature range (Figure S9a) show three field-induced

transitions, at \sim 1, \sim 6.1, and \sim 7.1 T at 2 K. These transitions are more easily seen in a dM/dH plot (Figure S9b). At 9 T, M reaches 3.4 $\mu_{\rm B}$ /Tb, a value about one third that of the 9 $\mu_{\rm B}$ of the saturated Tb moment.

To investigate the magnetic structure, we performed NPD at 8, 22, and 100 K. Figure 6d,e shows the magnetic scattering obtained by subtracting the pattern at 100 K (Figure 1j). Below $T_{\rm NI}$, additional magnetic peaks appear. These peaks can be indexed using the propagation vector, $\mathbf{k} = (0, 1/2, 0)$. After checking all possible magnetic models (described in detail in Section S6), the best refinement with magnetic $R_{\text{MAG}} = 7.2\%$ was obtained by the 1st, 2nd, and 3rd basis vectors of irreducible representation Γ_2 . The refined magnetic moment of half of the Tb at 8 K is 4.9(2) μ_B . The other half of the Tb atoms is nonmagnetic. A schematic of the alternating planes of magnetic and nonmagnetic Tb is shown in the upper sketch in Figure 6f. At 22 K, between T_{N1} and T_{N2} , additional peaks appear. These new Bragg peaks are inconsistent with any commensurate magnetic structure. The propagation vector that gives the best agreement is k = (0, 0.605, 0). The best solution was obtained by considering the 1st, 3rd, and 4th basis vectors of the irreducible representation Γ_2 , with $R_{\text{MAG}} =$ 12.16%. The solution with 1st, 3rd, and 6th basis vectors gives comparable agreement to the observed NPD, with R_{MAG} = 12.20%. The magnetic model corresponds to a sinewave-like structure. The refined magnetic moment oscillates from 0 $\mu_{\rm B}$ up to 5.0(2) $\mu_{\rm B}$. A schematic of this structure is shown in the lower panel in Figure 6f.

The apparent nonmagnetic state of every second Tb atom follows the sinewave modulation for this structure. These particular Tb atoms are positioned in the nodes of that modulation causing their magnetic moments to cancel. This does not happen for the incommensurate $\mathbf{k}=(0,\,0.605,\,0)$ structure by geometrical considerations.

From the results shown in Figure S6e, a small, negative $\theta = -12.1$ K and $\mu_{\rm eff} = 9.78(3)$ $\mu_{\rm B}$ are obtained for the Tb phase. The M is not saturated at 9 T and reaches only 3.4 $\mu_{\rm B}$. Here againthe reduction of magnetic moment is likely due to CEF interaction. ³¹

 $(Mo_{2/3}Er_{1/3})_2AlC$. A plot of M/H versus T for this phase, at H=0.01 T, is shown by a solid line in Figure 7a (left y-axis). A magnetic transition is barely visible. However a pronounced lambda anomaly in c_p (right y-axis in Figure 7a) is observed at $T_N=3.6$ K. The M versus H curves (Figure 7b) show no hysteresis and no remanence. The magnetization approaches $\sim 6~\mu_B/{\rm Er}$ at 9 T. At 2 K (black line in Figure 7b), a kink can be seen at ~ 1 T, implying a field-induced transition. Figure S6g shows the fitting of H/M versus T to the Curie—Weiss law resulting in 9.24(1) μ_B per Er atom, a value that is close to the free ion effective value.

When the NPD data at 298 (not shown) and 22 K (Figure 7c) were compared, no evidence for any structural transitions was seen. The LPs of all three axes decreased upon cooling. The unit cell volume contracted by 0.45%, which is typical of the *i*-MAX phases.³² Upon cooling below 3.6 K, however, the phase magnetically orders and new reflections emerge, that do not coincide with the crystal structure. The magnetic scattering spectrum of the Er phase at 1.5 K (Figure 7d) is obtained by subtracting the 22 K profile (Figure 7c).

Attempts to fit the diffraction pattern at 1.5 K using propagation vectors that belong to special symmetry points in the Brillouin zone resulted in propagation vector $\mathbf{k_1} = (1/2, 0, 1/2)$. This only accounted for part of the magnetic structure.

To fit the remaining magnetic structure, a systematic search of k along lines within the Brillouin zone, combined with a Monte Carlo refinement of the spin configuration at each k, was performed using the SARAh code. The incommensurate propagation vector $\mathbf{k}_2 = (0, 0.675(1), 0)$ successfully indexed the remaining magnetic reflections. The details are described in Section S6. The ordered magnetic moments corresponding to the \mathbf{k}_1 and \mathbf{k}_2 structures were refined to be 1.00(3) ($R_{\text{MAG}} = 11.2\%$) and 5.6(2) μ_{B}/Er ($R_{\text{MAG}} = 10.3$), respectively. The two proposed stuctures are sketched in in Figure 7e and f. Importantly, like in the Tb case, the Er ordered magnetic moment is significantly reduced compared to the Er³+ free ion moment (9 μ_{B}), most probably due to similar considerations.

DISCUSSION AND CONCLUSIONS

In the sixties, Nowotny et al. discovered, in powder form, roughly 50 MAX phases. The original set of M elements was Ti, Nb, Zr, Hf, V, Mo, Ta, and Cr. These phases were then mostly ignored for the next two decades. Interest in these phases was revitalized in the mid-nineties and has since remained high. In 2013 we discovered the first magnetic MAX phase and added Mn to the original set of M elements. In 2017 and 2018, we discovered the *i*-MAX phases, which added Sc, Y, and W to the mix. The only study on a RE MAX phase was on the superconductivity of Lu₂SnC. Herein, we add 11 new elements and essentially double the known MAX-phase M elements by realizing a new class of RE-based magnetic *i*-MAX phases.

These phases display a wide range of magnetic characteristics, ranging from incommensurate magnetic structures, to magnetization plateaus, to multi-k structures. We suggest that this behavioral variety is a result of competing long ranged exchange interactions in the presence of magnetocrystalline anisotropy. Various noncollinear AFM states are found in these phases, in particular for the Tb and Er phases.

Recently, reports on 2D magnetic materials (monolayers of Cr₂Ge₂Te₆ and CrI₃) have appeared in the literature, displaying layer-dependent magnetic phenomena. ^{39,40} The vast majority of all MXenes (the 2D derivative of the MAX phases) to date originate from selective etching of the Al layer from a MAX phase. ⁴¹ This concept was recently expanded by selectively etching both Al and Sc from (Mo_{2/3}Sc_{1/3})₂AlC *i*-MAX, resulting in a new 2D solid with ordered divacancies. ¹⁶ Furthermore, "targeted etching" was proposed for the (Mo_{2/3}Y_{1/3})₂AlC *i*-MAX, showing evidence for etching procedures resulting in vacancy formation or the realization of chemically ordered MXenes based on Mo and Y. ⁴² All novel *i*-MAX phases presented herein are Al based. Therefore, at least in principle, it should be possible to convert them to their 2D counterparts, which is ongoing.

Herein we report the synthesis of a MAX-phase based, RE-containing, family of ordered, layered solids, with complex inter- and intraplanar magnetic order. The chemistry of this family is $(Mo_{2/3}RE_{1/3})_2AlC$, with the RE atoms positioned at the apexes of a 2D triangular lattice. Eleven phases were discovered for RE, namely, Ce, Pr, Nd, Sm, Gd, Tb, Dy, Ho, Er, Tm, and Lu, which crystallize in three polymorphs with C2/c, C2/m, and Cmcm symmetries. The 2D metal carbide blocks are identical. We thus label this family RE i-MAX. Using Tb and Er quaternaries as examples we demonstrate the complex magnetic order, characteristic of magnetically frustrated systems due to competing intra- and in-plane magnetic interactions. Both structures contain incommensu-

rate as well as commensurate magnetic modulations depending on temperature. Interestingly, the incommensurate structures of the Tb and Er compounds are similar, while the commensurate ones differ albeit sharing the same crystallographic symmetry. This suggests a strong dependency of magnetic interactions on the RE atoms as well. The prospect that some of these phases may be converted to their 2D counterparts ⁴² adds to their potential importance.

ASSOCIATED CONTENT

S Supporting Information

The Supporting Information is available free of charge on the ACS Publications website at DOI: 10.1021/acs.chemmater.8b05298.

Crystal structure from STEM and XRD. Relationship between the three polymorphs. Theoretical modeling. Curie-Weiss fitting in the paramagnetic state. Magnetism of $(Mo_{2/3}Gd_{1/3})_2AlC$ and $(Mo_{2/3}Tb_{1/3})_2AlC$. Detailed magnetic structure analysis of the NPD data. Structural parameters from NPD. Crystal structure of RE MAX. Rietveld refinement of XRD. Schematic illustration of different stacking sequences for RE MAX. Schematic representation of six collinear spin configurations. Local magnetic moment of RE. H/M versus T and fitting to the Curie-Weiss law. Magnetic behavior of $(Mo_{2/3}Gd_{1/3})_2AlC$. Heat capacity and magnetic entropy. Magnetism of (Mo_{2/3}Tb_{1/3})₂AlC. Cell parameters and atom coordinates obtained from XRD Rietveld refinement. Phase purity from Rietveld refinement. Structural refinement from NPD (PDF)

AUTHOR INFORMATION

Corresponding Authors

*E-mail: quanzheng.tao@liu.se (Q.T.). *E-mail: johanna.rosen@liu.se (J.R.).

ORCID ®

Quanzheng Tao: 0000-0002-4073-5242 Martin Dahlqvist: 0000-0001-5036-2833 Michel W. Barsoum: 0000-0001-7800-3517 Johanna Rosen: 0000-0002-5173-6726

Author Contributions

J.R. initiated and supervised the study. Q.T., A.P., and R.M. conducted the synthesis. Q.T. and E.N.C. performed XRD analysis. L.H. oversaw the MAX phase STEM analysis performed by J.L. M.D. performed the ab initio calculations, with B.J. providing guidance. Q.T., A.M., S.C., O.R., D.P., E.N.C., H.S., A.H., C.R., and A.R.W. contributed to the neutron experiment and analysis. Q.T., C.O., R.-M.G., R.S., U.W., and M.F. contributed to the magnetic characterizations. Q.T., M.F., M.W.B., and J.R. wrote the manuscript with contributions from the other co-authors. All co-authors read and commented on successive drafts of the manuscript.

Notes

The authors declare no competing financial interest.

ACKNOWLEDGMENTS

J.R., P.P., and L.H. acknowledge support from the Knut and Alice Wallenberg (KAW) Foundation for a Scholar Grant, a Fellowship Grant, Project funding (KAW 2015.0043), and for support to the Linköping Ultra Electron Microscopy Laboratory. The Swedish Research Council is gratefully

acknowledged through Projects 642-2013-8020, 2015-00607, and 621-2014-4890. The calculations were carried out using supercomputer resources provided by the Swedish National Infrastructure for Computing (SNIC) at the National Supercomputer Centre (NSC), the High Performance Computing Center North (HPC2N), and the PDC Center for High Performance Computing. J.R. and P.P. also acknowledge the Swedish Government Strategic Research Area in Materials Science on Functional Materials at Linköping University (Faculty Grant SFO-Mat-LiU No. 2009-00971). R.S. acknowledges DFG funding under Grant SA 3095/2-1. A portion of this research used resources at the High Flux Isotope Reactor, a DOE Office of Science User Facility operated by the Oak Ridge National Laboratory. We thank HZB for the allocation of neutron radiation beamtime. D.P., O.R., and E.N.C. acknowledge the support of the IAEC Pazy Foundation Grant. M.B. was supported by NSF (DMR-1740795),

REFERENCES

- (1) Riseborough, P. S. Heavy fermion semiconductors. *Adv. Phys.* **2000**, *49*, 257–320.
- (2) Dzero, M.; Xia, J.; Galitski, V.; Coleman, P. Topological Kondo insulators. *Annu. Rev. Condens. Matter. Phys.* **2016**, *7*, 249–280.
- (3) Xu, Y.; Yue, C.; Weng, H.; Dai, X. Heavy Weyl Fermion State in CeRu₄ Sn₆. *Phys. Rev. X* **2017**, *7*, No. 011027.
- (4) Brando, M.; Belitz, D.; Grosche, F. M.; Kirkpatrick, T. R. Metallic quantum ferromagnets. *Rev. Mod. Phys.* **2016**, 88, No. 025006.
- (5) Wirth, S.; Steglich, F. Exploring heavy fermions from macroscopic to microscopic length scales. *Nat. Rev. Mater.* **2016**, *1*, 16051.
- (6) Tsujimoto, M.; Matsumoto, Y.; Tomita, T.; Sakai, A.; Nakatsuji, S. Heavy-fermion superconductivity in the quadrupole ordered state of PrV_2Al_{20} . *Phys. Rev. Lett.* **2014**, *113*, 267001.
- (7) Akintola, K.; Pal, A.; Potma, M.; Saha, S. R.; Wang, X. F.; Paglione, J.; Sonier, J. E. Quantum spin fluctuations in the bulk insulating state of pure and Fe-doped SmB₆. *Phys. Rev. B* **2017**, 95, 245107.
- (8) Sanada, S.; Aoki, Y.; Aoki, H.; Tsuchiya, A.; Kikuchi, D.; Sugawara, H.; Sato, H. Exotic heavy-fermion state in filled Skutterudite SmOs₄Sb₁₂. *J. Phys. Soc. Jpn.* **2005**, *74*, 246–249.
- (9) Lu, F.; Zhao, J.; Weng, H.; Fang, Z.; Dai, X. Correlated topological insulators with mixed valence. *Phys. Rev. Lett.* **2013**, *110*, No. 096401.
- (10) Barsoum, M. W. The $M_{\rm N+1}AX_{\rm N}$ phases: A new class of solids: Thermodynamically stable nanolaminates. *Prog. Solid State Chem.* **2000**, 28, 201–281.
- (11) Barsoum, M. W.; Radovic, M. Elastic and mechanical properties of the MAX phases. *Annu. Rev. Mater. Res.* **2011**, *41*, 195–227.
- (12) Barsoum, M. W. MAX phases: properties of machinable ternary carbides and nitrides. John Wiley & Sons: 2013, DOI: 10.1002/9783527654581.
- (13) Fashandi, H.; Dahlqvist, M.; Lu, J.; Palisaitis, J.; Simak, S. I.; Abrikosov, I. A.; Rosen, J.; Hultman, L.; Andersson, M.; Spetz, A. L.; Eklund, P. Synthesis of $\mathrm{Ti_3AuC_2}$, $\mathrm{Ti_3Au_2C_2}$ and $\mathrm{Ti_3IrC_2}$ by noble metal substitution reaction in $\mathrm{Ti_3SiC_2}$ for high-temperature-stable Ohmic contacts to SiC. *Nat. Mater.* **2017**, *16*, 814–818.
- (14) Naguib, M.; Kurtoglu, M.; Presser, V.; Lu, J.; Niu, J.; Heon, M.; Hultman, L.; Gogotsi, Y.; Barsoum, M. W. Two-dimensional nanocrystals produced by exfoliation of Ti₃AlC₂. *Adv. Mater.* **2011**, 23, 4248–4253.
- (15) Anasori, B.; Lukatskaya, M. R.; Gogotsi, Y. 2D metal carbides and nitrides (MXenes) for energy storage. *Nat. Rev. Mater.* **2017**, *2*, 16098.
- (16) Tao, Q.; Dahlqvist, M.; Lu, J.; Kota, S.; Meshkian, R.; Halim, J.; Palisaitis, J.; Hultman, L.; Barsoum, M. W.; Persson, P. O. Å.; Rosen,

J. Two-dimensional $Mo_{1.33}C$ MXene with divacancy ordering prepared from parent 3D laminate with in-plane chemical ordering. *Nat. Commun.* **2017**, *8*, 14949.

- (17) Dahlqvist, M.; Lu, J.; Meshkian, R.; Tao, Q.; Hultman, L.; Rosen, J. Prediction and synthesis of a family of atomic laminate phases with Kagomé-like and in-plane chemical ordering. *Sci. Adv.* **2017**. 3, No. e1700642.
- (18) Meshkian, R.; Dahlqvist, M.; Lu, J.; Wickman, B.; Halim, J.; Thörnberg, J.; Tao, Q.; Li, S.; Intikhab, S.; Snyder, J.; Barsoum, M. W.; Yildizhan, M.; Palisaitis, J.; Hultman, L.; Persson, P. O. Å.; Rosen, J. W-Based Atomic Laminates and Their 2D Derivative W_{1.33}C MXene with Vacancy Ordering. *Adv. Mater.* **2018**, *30*, 1706409.
- (19) Kresse, G.; Hafner, J. Ab initio molecular dynamics for liquid metals. *Phys. Rev. B* **1993**, *47*, 558–561.
- (20) Kresse, G.; Furthmüller, J. Efficiency of ab-initio total energy calculations for metals and semiconductors using a plane-wave basis set. *Comput. Mater. Sci.* **1996**, *6*, 15–50.
- (21) Kresse, G.; Furthmüller, J. Efficient iterative schemes for ab initio total-energy calculations using a plane-wave basis set. *Phys. Rev.* B **1996**, *54*, 11169–11186.
- (22) Blöchl, P. E. Projector augmented-wave method. *Phys. Rev. B* **1994**, *50*, 17953–17979.
- (23) Kresse, G.; Joubert, D. From ultrasoft pseudopotentials to the projector augmented-wave method. *Phys. Rev. B* **1999**, *59*, 1758–1775.
- (24) Perdew, J. P.; Burke, K.; Ernzerhof, M. Generalized gradient approximation made simple. *Phys. Rev. Lett.* **1996**, *77*, 3865–3868.
- (25) Monkhorst, H. J.; Pack, J. D. Special points for Brillouin-zone integrations. *Phys. Rev. B* **1976**, *13*, 5188–5192.
- (26) Dudarev, S. L.; Botton, G. A.; Savrasov, S. Y.; Humphreys, C. J.; Sutton, A. P. Electron-energy-loss spectra and the structural stability of nickel oxide: An LSDA+U study. *Phys. Rev. B* **1998**, *57*, 1505–1509.
- (27) Gschneidner, K. A. Physical properties of the rare earth metals. *Bull. Alloy Phase Diagrams* **1990**, *11*, 216–224.
- (28) Hughes, I. D.; Däne, M.; Ernst, A.; Hergert, W.; Lüders, M.; Poulter, J.; Staunton, J. B.; Svane, A.; Szotek, Z.; Temmerman, W. M. Lanthanide contraction and magnetism in the heavy rare earth elements. *Nature* **2007**, *446*, 650–653.
- (29) Farle, M.; Lewis, W. A.; Baberschke, K. Detailed analysis of the in situ magneto-optic Kerr signal of gadolinium films near the Curie temperature. *Appl. Phys. Lett.* **1993**, *62*, 2728–2730.
- (30) Opagiste, C.; Jackson, M. J.; Galéra, R.-M.; Lhotel, E.; Paulsen, C.; Ouladdiaf, B. Metamagnetic behaviour of Nd₃Pt₂₃Si₁₁. *J. Magn. Magn. Mater.* **2013**, 340, 46–49.
- (31) Rivin, O.; Osborn, R.; Kolesnikov, A. I.; Caspi, E. N.; Shaked, H. Tb³⁺ in TbCo₃B₂: A singlet ground state system studied by inelastic neutron scattering. *Phys. Rev. B* **2008**, *78*, 184424.
- (32) Caspi, E. N.; Chartier, P.; Porcher, F.; Damay, F.; Cabioc'h, T. Ordering of (Cr, V) Layers in Nanolamellar (Cr_{0.5}V_{0.5})_{n+1}AlC_n Compounds. *Mater. Res. Lett.* **2015**, 3, 100–106.
- (33) Wills, A. S. A new protocol for the determination of magnetic structures using simulated annealing and representational analysis (SARAh). *Phys. B* **2000**, 276-278, 680–681.
- (34) Wills, A. S. Indexing magnetic structures and crystallographic distortions from powder diffraction: Brillouin zone indexing. *Z. Kristallogr. Suppl.* **2009**, *30*, 39–44.
- (35) Schuster, J. C.; Nowotny, H.; Vaccaro, C. The ternary systems: CrAlC, VAlC, and TiAlC and the behavior of H-phases (M2AlC). *J. Solid State Chem.* **1980**, 32, 213–219.
- (36) Barsoum, M. W.; El-Raghy, T. Synthesis and characterization of a remarkable ceramic: Ti₃SiC₂. *J. Am. Ceram. Soc.* **1996**, *79*, 1953–1956.
- (37) Ingason, A. S.; Mockute, A.; Dahlqvist, M.; Magnus, F.; Olafsson, S.; Arnalds, U. B.; Alling, B.; Abrikosov, I. A.; Hjörvarsson, B.; Persson, P. O. Å.; Rosen, J. Magnetic self-organized atomic laminate from first principles and thin film synthesis. *Phys. Rev. Lett.* **2013**, *110*, 195502.

(38) Kuchida, S.; Muranaka, T.; Kawashima, K.; Inoue, K.; Yoshikawa, M.; Akimitsu, J. Superconductivity in Lu₂SnC. *Phys. C* **2013**, 494, 77–79.

- (39) Huang, B.; Clark, G.; Navarro-Moratalla, E.; Klein, D. R.; Cheng, R.; Seyler, K. L.; Zhong, D.; Schmidgall, E.; McGuire, M. A.; Cobden, D. H.; Yao, W.; Xiao, D.; Jarillo-Herrero, P.; Xu, X. Layer-dependent ferromagnetism in a van der Waals crystal down to the monolayer limit. *Nature* **2017**, *546*, 270–273.
- (40) Gong, C.; Li, L.; Li, Z.; Ji, H.; Stern, A.; Xia, Y.; Cao, T.; Bao, W.; Wang, C.; Wang, Y.; Qiu, Z. Q.; Cava, R. J.; Louie, S. G.; Xia, J.; Zhang, X. Discovery of intrinsic ferromagnetism in two-dimensional van der Waals crystals. *Nature* **2017**, *546*, 265–269.
- (41) Naguib, M.; Mashtalir, O.; Carle, J.; Presser, V.; Lu, J.; Hultman, L.; Gogotsi, Y.; Barsoum, M. W. Two-dimensional transition metal carbides. *ACS Nano* **2012**, *6*, 1322–1331.
- (42) Persson, I.; el Ghazaly, A.; Tao, Q.; Halim, J.; Kota, S.; Darakchieva, V.; Palisaitis, J.; Barsoum, M. W.; Rosen, J.; Persson, P. O. Å. Tailoring Structure, Composition, and Energy Storage Properties of MXenes from Selective Etching of In-Plane, Chemically Ordered MAX Phases. *Small* **2018**, *14*, 1703676.